The structural versatility of proton sponge bismuth halides

Gonzalo García-Espejo, [a] Candida Pipitone,[b] Francesco Giannici, [b] Norberto Masciocchi [a,*]

[a] Dipartimento di Scienza e Alta Tecnologia and To.Sca.Lab, Università dell'Insubria, via Valleggio 11, 22100 Como (Italy).

[b] Dipartimento di Fisica e Chimica "Emilio Segrè", Università di Palermo, viale delle Scienze, 90128 Palermo (Italy).

* Corresponding author:

E-mail address: norberto.masciocchi@uninsubria.it (N. Masciocchi)

ABSTRACT

Hybrid halometalates containing lead, tin, bismuth and antimony have recently shown a bevy of interesting photophysical properties. Aiming at finding chemically stable and thermally inert species, three halobismutate species of this class, crystallized with proton sponge-derived cations (PRSH), have been isolated as microcrystalline powders by mixing 1,8-bis(dimethylamino)-naphthalene and bismuth oxide in concentrated HX acids (X = Cl, Br and I). The two isomorphous $(PRSH)_3Bi_2X_9$ (X = Br, I) species, containing isolated $[Bi_2X_9]^{3-}$ anions, are triclinic at room temperature and convert upon heating into a monoclinic structure through a displacive phase transformation, fully reversible for X = I and only partially for X = Br. At variance, $(PRSH)BiCl_4$ is polymeric, and contains extended zigzagging 1D chains formed by edge-sharing $BiCl_6$ octahedra. These species were extensively studied by synchrotron and laboratory X-ray powder diffraction measurements, which enabled to detect the evolution toward the two high-temperature β-phases (X = Br, I), to derive the structure of five different (significantly complex) species and to assess the thermal strain tensors in the different regimes. Additional thermal, spectroscopic and computational analyses completed the characterization of these materials.

KEYWORDS: Bismuth halides, proton sponge, synchrotron X-rays, crystal structure, powder diffraction.

1. Introduction

The last decade has witnessed a rejuvenation of the haloplumbate materials, particularly of the 3D perovskite type,[1] for their excellent photophysical, thermoelectric, lasing and hard electromagnetic radiation detection properties. [2,3] These studies opened the way to a number of new applications, in the displays, sensors, and other optoelectronic fields. [4,5,6] Typically, these materials possess, as small counterions, either inorganic (akin Cs^+) or organic (methylammonium, MA; formamidinium, FA) species, filling the cuboctahedral hole, and surrounded by 12 halides. [7] Prompted by the partial instability in environmental conditions of some of these species, [8] and particularly of their organic ligand-stabilized nanocrystalline version, low dimensional haloplumbates, where (larger) organic cations are inserted as spacers, have been studied, and new crystal phases with layers, ribbons or rods of PbX_n^{n-2} formulation have been widely prepared. [9] Among them, Ruddlesen-Popper[10] and Dion-Jacobson[11] systems (of ideal $A_{n+1}Pb_nX_{3n+1}$ or $A_{n-1}A'Pb_nX_{3n+1}$ stoichiometry, respectively – with A and A′ = mono- and divalent cations, and X = halide) have shown the most interesting photophysical properties, coupled to a higher chemical and thermal stability, but other systems, with edge, corner or face sharing octahedra have also been isolated.

In search for alternative species avoiding the use of the toxic Pb ions is,[12] (halo)stannates, bismutates and antimonates recently entered the field, some of them showing 3D connectivity, but, more often, lower dimensionality systems, mostly related to charge balancing effects if trivalent metals are employed. [13] The main feature of these species is the persistency of octahedral halide (X) coordination of the metals (M), which can give rise to isolated mononuclear or oligomeric ions, or more extended moieties, depending on the M:X stoichiometric ratio and on the bulkiness and steric requirements of the organic cations (A). Indeed, to some extent, the rich crystal-chemical versatility of the $A_nB_mX_p$ species parallels that of silicates, ranging from ortho-SiO_4^{4-}tetrahedra to SiO_2 polymorphs (or framework silicates), with all intermediate cyclo-, ino- and phyllo-silicates (and their combinations) in between.[14] Finally, an additional parameter which influences the crystalline and physical properties of these systems in also the deliberate doping,[15] which can occur at the A site

[*e.g.*, $(Cs,FA)PbX_3$)], [16] in the halides [*e.g.*, $(PRSH)Pb(Br,X)_3$] [17] (PRSH = protonated 1,8-bis(dimethylamino)-naphthalene or *proton sponge*] or even at the framework metal site [*e.g.*, $(TMSO)_3Pb_{2x},Bi_{2(1-x)}X_9$], [18] $0 \leq x \leq 1$, TMSO = trimethylsulfoxonium].

Replacement of lead by bismuth in organic-inorganic metal halides hybrids was recently proposed as a green and reasonably cost-effective strategy (compared to alternative solutions), also because of the similarity of electronic and steric requirements shared by Pb(II) and Bi(III) ions. [19] In addition, Bi(III) manifests a higher stability towards moisture[20] and oxidation (Bi_2O_5 possessing a higher standard reduction potential than PbO_2[21]), and a few low-dimensional hybrid halobismutates have been prepared, with interesting optoelectronic performances (narrow band gaps and long-lived photoluminescence[22]) and excellent light-absorption properties in a wide portion of the visible range. [23] Prompted by these results, and following our studies of PRSH-based 1D-haloplumbates, we turned now our attention to the Bi(III) halide series, the preparation and characterization of which are reported hereafter.

2. Experimental Section

2.1 Materials

Bismuth oxide (Bi_2O_3, 99.9 %), proton sponge (1,8-bis(dimethylamino)naphthalene: $C_{10}H_6(N(CH_3)_2)_2$, 99 %), hydrobromic acid (HBr, 48 % w/w in H_2O) and hydroiodic acid (HI, 57 % w/w in H_2O) were purchased from Sigma-Aldrich/Merck. Hydrochloric acid (HCl, 37 % w/w in H_2O) was purchased from VWR Chemicals. All reagents were used as received without any further purification.

2.2 Syntheses

2.2.1 (PRSH)$BiCl_4$

Bi_2O_3 powder (0.5 mmol) was dissolved in 3 mL of HCl solution by stirring and heating the mixture up to 70 °C. Subsequent addition of PRS powder (1 mmol) caused the immediate precipitation of a white solid. The precipitate was redissolved under vigorous stirring and heating the

solution up to boiling. Then, stirring was discontinued, and the solution was left to slowly cool to room temperature overnight, during which time a white precipitate started to crystallize. Finally, the crystals were collected and dried by filtration under vacuum.

2.2.2 $(PRSH)_3Bi_2Br_9$

Bi_2O_3 powder (0.5 mmol) was dissolved in 6 mL of HBr solution by stirring and heating the mixture up to 70 °C. Subsequent addition of PRS powder (1 mmol) caused the immediate precipitation of a yellow solid. The precipitate was redissolved under vigorous stirring and heating the solution up to boiling. Then, stirring was discontinued, and the solution was left to slowly cool to room temperature overnight, during which time a bright yellow precipitate started to crystallize. Finally, the crystals were collected and dried by filtration under vacuum. This material, labelled as the $(PRSH)_3Bi_2Br_9$ α-phase, can be easily and quantitatively transformed by gentle heating (slightly below 100°C) into a high-temperature β-phase. Upon cooling to RT, and measuring its XRD pattern, the β-phase is found to be stable for a couple of hours. On the following day, a mixture of α- and β-phases is observed, which is stable in such a mixed form for at least 2 months (and probably forever).

2.2.3 $(PRSH)_3Bi_2I_9$

Bi_2O_3 powder (0.5 mmol) was dissolved in 6 mL of HI solution by stirring and heating the mixture up to 80 °C. Subsequent addition of PRS powder (1 mmol) caused the immediate precipitation of an intense red solid. By vigorous stirring and heating the solution up to its boiling point, we tried to redissolve the precipitate, but found it impossible under the current conditions. Therefore, stirring was discontinued, and the solution was left to slowly cool down to room temperature. Finally, the crystals were collected and dried by filtration under vacuum. This material, labelled as the $(PRSH)_3Bi_2I_9$ α-phase, can be easily and quantitatively transformed by gentle heating (slightly below 150°C) into a high-temperature β-phase. Upon cooling to RT, full reversibility to the α-phase is observed within minutes.

2.2.4 Caution

Even though no problem was encountered in the course of this research, concentrated aqueous solutions of hydroiodic and hydrobromic acids are potentially harmful (both as solutions and as fumes), particularly when heated well above 100°C during the syntheses. Properly working fume hoods and careful handling procedures must be guaranteed.

2.3 Characterization procedures

2.3.1 Thermal analyses

Thermogravimetric (TG) traces were acquired from 30 to 300°C (with a scan rate of 10 °C min^{-1}) using a STA 409 PC Luxx® analyzer (Netzsch) under a nitrogen flow and with alumina sample holders equipped with a pierced lid.

2.3.2 Diffuse reflectance spectroscopy

UV-vis-NIR reflectance spectra of the powders, R, were measured in the 200-800 nm range using a UV-2600 Shimadzu spectrometer. $BaSO_4$ was used as non-absorbing reflectance reference. The Kubelka-Munk function F[R] was calculated from the reflectance spectrum, using the $F[R] = (1 - R)^2/2R$ relationship. Taking F[R] as the representative of the sample absorbance spectrum, extrapolation of the linear portion of the $(F[R]\ h\nu)^2$ vs $h\nu$ plot on the $h\nu$ axis provided experimentally accessible band gap values (Tauc plots[24]).

2.3.3 X-ray fluorescence

Gently ground powders of the three crystalline α-phases were deposited on a polycarbonate film and analyzed with a MiniPal2 XRF spectrometer (PANalytical), working with a Cr-anode at 30 kV and 2 µA. X-ray fluorescence lines were measured for Bi (L_α and L_β lines, at 10.8 and 13.0 keV, respectively), Cl (K_α and K_β lines, at 2.6 and 2.8 keV, respectively), Br (K_α and K_β lines, at 11.9 and 13.3 keV, respectively) and I (L_α, $L_{\beta1}$, $L_{\beta2}$ and L_γ lines, at 3.93, 4.22, 4.51 and 4.80 keV, respectively). Intensity calibration for Bi/Cl in $(PRSH)BiCl_4$ was performed using an equimolar amount of Bi and Cl, through a mixture of Bi_2O_3 and MACl (MA = methylammonium); in this case, partial overlap of the *K*(Cl) and *M*(Bi) emission lines made it difficult to reach high analytical accuracy. In the case of

Bi/Br in $(PRSH)_3Bi_2Br_9$, pristine $BiBr_3$ powder was used instead for calibration, and for the Bi/I ratio in $(PRSH)_3Bi_2I_9$, an equimolar amount of Bi and I was employed, using a mixture of Bi_2O_3 and CuI.

2.4 X-ray diffraction analysis

Powders of the α-phases were gently ground in agate mortar, loaded in a G50 capillary, sealed in air with epoxy-glue. X-ray diffraction data were collected at the MSX04SA beamline[25] of the Swiss Synchrotron using 22 keV radiation (λ = 0.564656 Å, calibrated with the use of a silicon powder standard, NIST SRM 640 d). Data were acquired in *ca.* 15 min time using the single photon counting MYTHEN II detector, [26] able to simultaneously cover the entire 1-120° angular range. Subtraction of the environmental scattering (air and capillary) and correction for absorption, using the μt value experimentally determined by radiographic exposure. were performed using a locally developed X-ray tracing protocol.

Standard peak search enabled the location of 20 low-angle peaks, typically falling in the 1-8° (or less) range, which were then fed to the Singular Value Decomposition[27] indexing algorithm of TOPAS-R, which provided the following results. For $(PRSH)BiCl_4$, Monoclinic P, a = 14.26, b = 18.30, c = 7.38 Å, β = 95.98°, GoF(20) = 169.4, for $(PRSH)_3Bi_2Br_9$, Triclinic P, a = 11.235, b = 13.53, c = 20.13 Å, α = 89.31, β = 86.05, γ = 115.30°, GoF(20) = 63.5, for $(PRSH)_3Bi_2I_9$, Triclinic P, a = 11.553, b = 13.91, c = 20.63 Å, α = 93.55, β = 86.23, γ = 113.86°, GoF(20) = 65.3. For the reasons discussed below, the last two triclinic cells were transformed, using the [-1,-2,0; -1,0,0; 0,0,-1] matrix, into C-centered analogues with double volume and used as such throughout the following discussion. Density considerations and systematic absences suggested space groups $P2_1/c$ $(PRSH)BiCl_4$ and C-1 for the two isomorphous $(PRSH)_3Bi_2X_9$ (X = Br, I) compounds (after transformation).

Structure solution was initiated by the simulated annealing technique using the 2-30° 2θ section only and freely floating Bi and halides (X), with soft restraints on the Bi-X bond distances and the Bi-coordination sphere. Once an approximate model was found for the complex anions, PRSH moieties were added as rigid bodies with idealized geometry (distances, angles and a few torsions),

with free center of mass location and molecular orientations. The final refinements were performed using all data up to 45° 2θ, corresponding to Q_{max} = 5.34 $Å^{-1}$, no evident scattering signal above background being observed beyond this value, and the coordinates of bismuth ions and all halides atoms were treated independently. No preferred orientation correction was necessary; a single isotropic displacement parameter was assigned to all atoms and the residual background modeled by a Chebyshev polynomial. Due to unavoidable limitations of the structural model of the organic moieties, which could not be refined by the independent atom model approach, some (too) short intermolecular H···H contacts exist, also because the torsional angles at the N-CH_3 linkages (6 occurrences) were kept fixed. A specific warning in this direction has also been included while depositing the CIF files within the CSD.

The β-phases were generated *in situ* in the diffractometer cradle, and measured in flat-plate conditions on a Bruker AXS D8 ADVANCE instrument, with nickel-filtered CuK$\alpha_{1,2}$ radiation and a position sensitive Lynxeye detector. Generator setting: 40 kV, 40 mA; Divergence slit: 0.5°. Scan-range: 3-105°; Δ2θ = 0.02°, t = 12 s $step^{-1}$. Indexing, structure solution and final refinements were performed as described above for the α-phases, with the obvious help of retrieving the final model from those of the α-phases by a displacive movement. In particular, indexing provided the following lattice parameters: for β-$(PRSH)_3Bi_2Br_9$, Monoclinic C, a = 24.16, b = 11.52, c = 19.90, β = 92.61, GoF(20) = 47.3; β-$(PRSH)_3Bi_2I_9$, Monoclinic C, a = 25.32, b = 11.87, c = 20.64, β = 91.87, GoF(20) = 22.6.

All X-ray diffraction-related computations were performed using the TOPAS-R suite of programs. [28] Figure 1 illustrates the final Rietveld refinement plots for all three room temperature species, while those of the β-phases are shown in in the Supporting Information, Figure S1. Crystal data and fractional atomic coordinates have been deposited at the Cambridge Crystallographic Data Center, CCDC Codes: 2153967-2153969.

Crystal data for (PRSH)BiCl₄: $C_{14}H_{19}BiCl_4N_2$, fw = 566.11 g mol^{-1}, monoclinic, $P2_1/c$, a = 14.2659(1), b = 18.3071(1), c = 7.38670(4) Å, β = 95.9798(4)°, V = 1918.67(2) Å^3, Z = 4, ρ_{calc} = 1.960 g cm^{-3}, μ(22 keV) = 60.1 cm^{-1}; R_p and R_{wp}, 0.055 and 0.061 respectively, 1.5-45° 2θ range. R_{Bragg} = 0.047.

Crystal data for α-(PRSH)₃Bi₂Br₉: $C_{42}H_{57}Bi_2Br_9N_6$, fw = 1783.04 g mol^{-1}, triclinic, C-1, a = 24.4462(2), b =11.2202(1), c = 20.0920(2) Å, α = 86.0536(6), β = 92.5230(6), γ = 89.1996(6)°, V = 5491.9(1) Å^3, Z = 4, ρ_{calc} = 2.156 g cm^{-3}, μ(22 keV) = 79.6 cm^{-1}; R_p and R_{wp}, 0.053 and 0.058 respectively, 1.5-45° 2θ range. R_{Bragg} = 0.074.

Crystal data for α-(PRSH)₃Bi₂I₉: $C_{42}H_{57}Bi_2I_9N_6$, fw = 2206.04 g mol^{-1}, triclinic, C-1, a = 25.4420(5), b = 11.5565(2), c = 20.6368(4) Å, α = 86.222(1), β = 92.125(1), γ = 89.312(1)°, V = 6049.7(2) Å^3, Z = 4, ρ_{calc} = 2.422 g cm^{-3}, μ(22 keV) = 63.9 cm^{-1}; R_p and R_{wp}, 0.072 and 0.083 respectively, 1.5-45° 2θ range. R_{Bragg} = 0.057.

Variable temperature X-ray diffraction (VTXRD) measurements were performed on a Bruker AXS D8 Advance diffractometer, using a custom made sample heater built by Officina Elettrotecnica di Tenno (Ponte Arche, TN, Italy). Data were collected in step scan mode, with Δ2θ = 0.02°, t = 1 s, and 2θ ranging from 5 to 30°, measuring the sample under isothermal condition and raising the temperature in 20 °C steps. Prolonged XRD measurements were performed at high enough temperatures (at 110 and 190 °C, for X = Br and I, respectively) on a Peltier-controlled sample heater equipped with a silicon zero-background plate (X = Br), or on an aluminum-based resistance-controlled hot stage (X = I), to stabilize the high-temperature monoclinic β-phases of $(PRSH)_3Bi_2I_9$ and $(PRSH)_3Bi_2I_9$. Both systems worked in air, and significant thermal gradients cannot be excluded. This is particularly the for the β-$(PRSH)_3Bi_2I_9$ phase, where some contamination of the (hot) α-polymorph is observable in the XRPD trace at low diffraction angles. Crystal data for the high-temperature phases are supplied in the Supplementary Text.

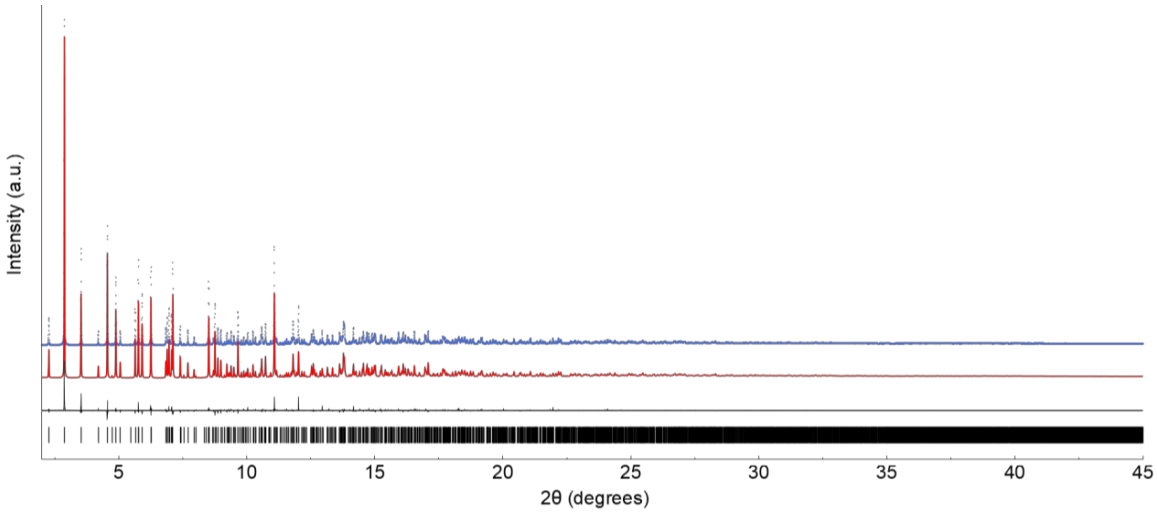

(a)

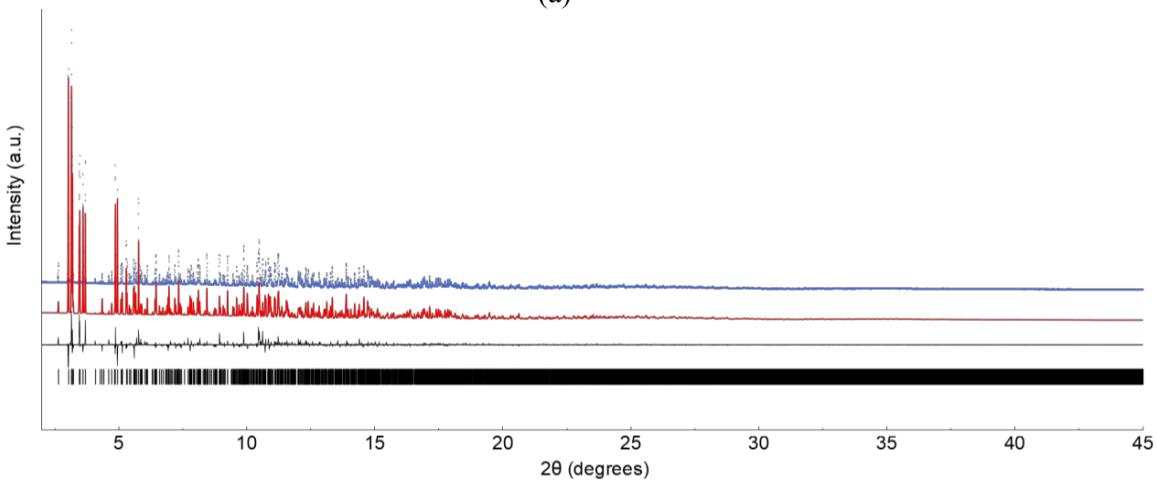

(b)

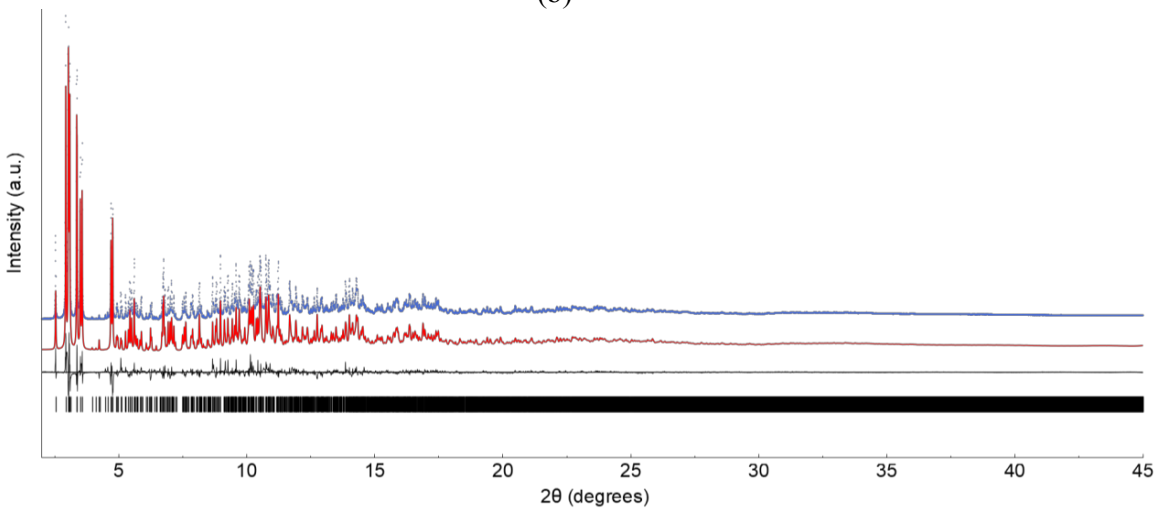

(c)

Figure 1. Rietveld refinement plots for $(PRSH)BiCl_4$ (a); α-$(PRSH)_3Bi_2Br_9$ (b) α-$(PRSH)_3Bi_2I_9$ (c). Raw data: blue dots; Calculated pattern: red line; difference plot and peak markers at the bottom.

2.5 Ab initio calculations

The electronic structures of $(PRSH)BiCl_4$, α-$(PRSH)_3Bi_2Br_9$ and α-$(PRSH)_3Bi_2I_9$ were calculated using periodic density functional theory (DFT) with the PWscf package in the Quantum Espresso suite, [29,30,31] adopting the PBE exchange-correlation functional,[32] with an energy cutoff of 60 Ry. Spin-orbit coupling was considered for Bi and all halide atoms. The crystal structure models of α-$(PRSH)_3Bi_2Br_9$ and α-$(PRSH)_3Bi_2I_9$ from X-ray diffraction were transposed from C-1 to P-1 setting, to halve the cell size. Such a volume reduction does not affect the description of the electronic structure. The band structure was calculated along the k-points path for triclinic symmetry obtained with SeeK-path. [33]

3. Results and Discussion

3.1 Crystal chemistry.

Crystals of $(PRSH)BiCl_4$ are monoclinic, $P2_1/c$, with all atoms lying in general positions. Therein, polymeric halobismutate chains, built by edge sharing BiI_6 octahedra linked in *cis*-position, run parallel to the **c** axis direction (see Figure 2). The polymeric $[BiCl_4^-]_\infty$ chains are separated by the PRSH cations, oriented in such a way that their formally charged portion (the $Me_2N\cdots H\cdots NMe_2$ fragment) points toward the terminal chlorides of the polyanion (not shown here). The intermetallic (non-bonding) Bi···Bi distance, of 4.34 Å, compares well with analogous distances retrieved from the CSD, which provided an average value of 4.28 Å for the $(\mu_2\text{-}Cl)_xBi_2$ fragment of edge-sharing octahedra (in *cis*-disposition). As expected, terminal Bi-Cl distances are ca. 0.3 Å shorter than for μ_2-Cl bridging ones (see Table 1). While some inevitable spread of distances and angles is typically found in structures retrieved from XRPD data only, the average values for the Bi-Cl and Bi-Cl-Bi reasonably match the values determined from conventional single-crystal diffraction analyses on analogous species. One may however note that the bridging chlorides are far from being symmetrically linked to the adjacent Bi ions (2.71 and 2.73 Å for the shortest distances, and 2.96 and 2.99 Å for the longest ones). These unexpected observation finds a strong confirmation in the crystal

structures of known analogues, [34-37] where shorter (avg. 2.73 Å) and longer (avg. 2.97 Å) values are *systematically* observed, and might attributed to the non-spherical shape of the Bi(III) ion, due to incipient and underestimated stereochemical activity of the $6s^2$ valence orbital. [38] *Inter alia*, this finding confirms the reliability of the details derived from our powder diffraction structural analysis.

Table 1. Synoptic collection of the most relevant geometrical parameters, together with the experimentally determined optical band gaps. Bold characters refer to the β-phases. The values in parentheses are the average values determined from a CSD search.

Parameter	$(PRSH)BiCl_4$	$(PRSH)_3Bi_2Br_9$	$(PRSH)_3Bi_2I_9$
Topology	Polymeric, *cis* corner sharing octahedra	Molecular, face sharing octahedra	Molecular, face sharing octahedra
Bi···Bi, Å	4.34 (4.29)	4.03 (3.99) **4.10**	4.17 (4.19) **4.09**
$<Bi\text{-}X_{term}>$, Å	2.56 (2.51)	2.75 (2.73) **2.71**	2.97 (2.95) **2.98**
$<Bi\text{-}X_{bridg}>$, Å	2.85 (2.81)	3.04 (3.03) **3.08**	3.26 (3.24) **3.18**
$<Bi\text{-}X_{bridg}\text{-}Bi>$, Å	99.3 (92.4)	82.9 (82.3) **83.3**	79.4 (80.4) **80.0**
Optical band-gap, eV	3.40	2.80	2.13

3.2 Spectroscopic Investigation

The colors of the powdered materials precipitated from solution clearly indicate that the electronic levels of their frontier orbitals of the three studied species are markedly different, and that the use of softer anions progressively lowers the optical absorption gaps. Obtained from reflectance measurements and analyzed by the Tauc plot method (see Figure 3), the optical band gap values, reported in Table 1, are fully in line with visual observations: $(PRSH)BiCl_4$ is white (E_g = 3.40 eV, in the UV region), $(PRSH)_3Bi_2Br_9$ canary yellow and $(PRSH)_3Bi_2I_9$ intense red (with absorption edges in the violet and cyan visible regions).

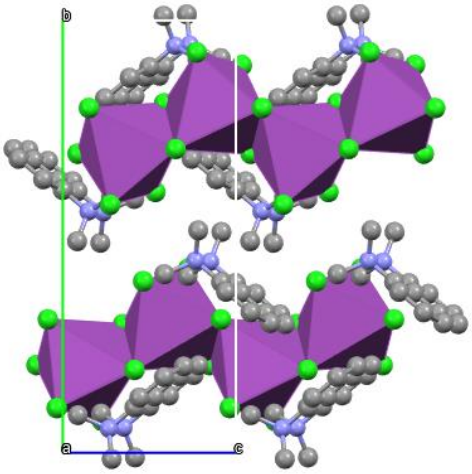

(a)

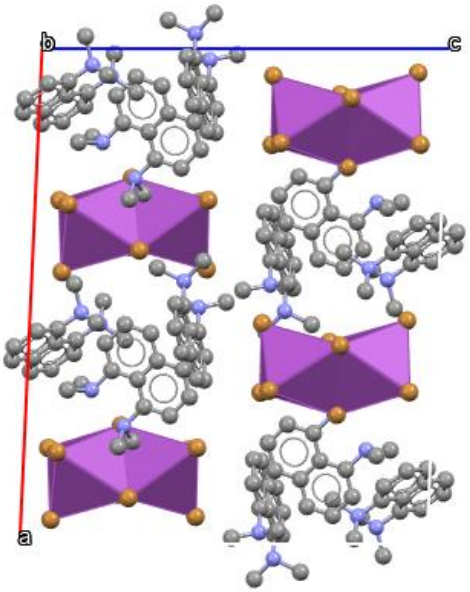

(b)

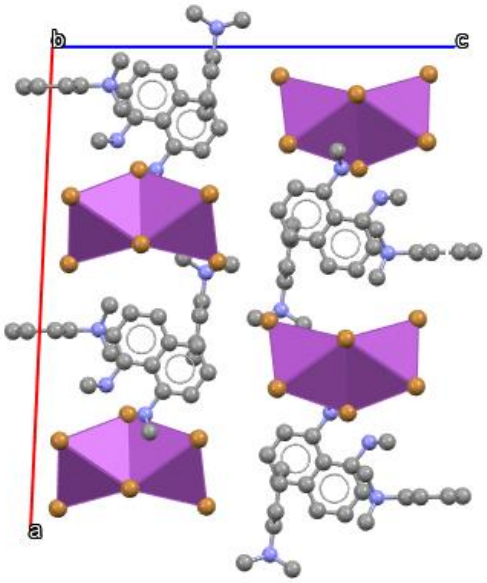

(c)

Figure 2. Packing diagram of the crystal structures of (PRSH)$BiCl_4$ (a) and $(PRSH)_3Bi_2Br_9$, α (b) and β (c) phases, with bismuth ion coordination highlighted in polyhedral representation. At the drawing resolution, the α- and β- $(PRSH)_3Bi_2I_9$ phases look similar to the isomorphous Br analogues. A polymeric sequence of corner-sharing octahedra is present in (PRSH)$BiCl_4$ (a), while in the $(PRSH)_3Bi_2Br_9$ species, isolated dinuclear $[Bi_2Br_9]^{2-}$ anions, with face-sharing octahedral, exist. Color codes: carbon (grey), nitrogen (blue), chloride (green) and bromine (brown). In all panels, hydrogen atoms are omitted for clarity. **a**, **b** and **c** axes are drawn as red, green and blue lines, respectively.

It is worth noting that the optical absorption spectra (and the band gap values derived therefrom) for $(PRSH)_3Bi_2Br_9$ and $(PRSH)_3Bi_2I_9$ are very similar to those of $[(CH_3)_3SO]_3Bi_2Br_9$ and $[(CH_3)_3SO]_3Bi_2I_9$, [18] which also display $[Bi_2X_9]^{3-}$ dimers, suggesting that influence of the organic cation on the electronic states close to the gap is irrelevant. This is also in line with the observation that during the thermal treatments no evident color change was detected, as the slight structural modifications occurring during the phase transformation maintain isolated $[Bi_2X_9]^{3-}$ anions.

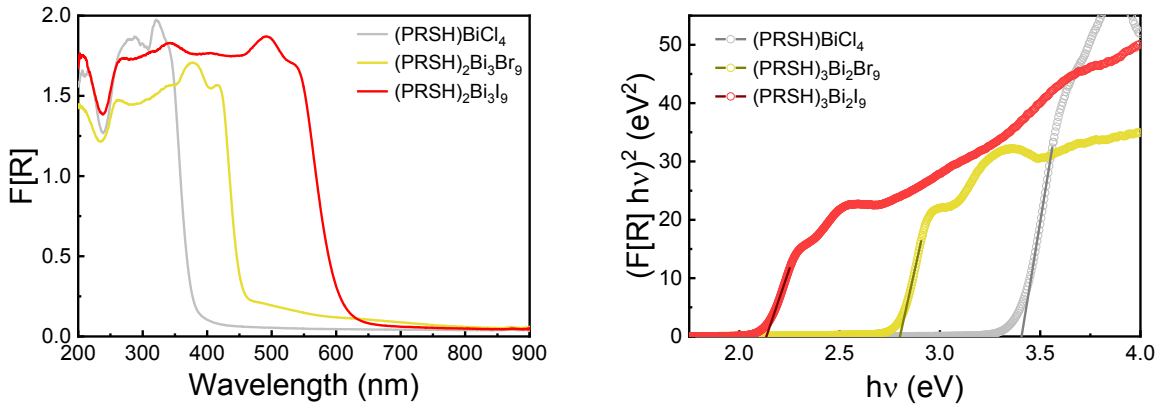

Figure 3. The Kubelka-Munk transformed UV-Vis reflectance spectra for the three species stable at RT (left); the derivation of the optical band gaps by the Tauc plot procedure (right).

3.3 Thermal Characterization

Variable-temperature X-ray diffraction (VTXRD, shown in Figure 4) provides a clear picture of the crystal phases (Figure 2) and lattice parameters (Figure 5) evolution upon raising the temperature, well before thermal decomposition. For $(PRSH)BiCl_4$, the monoclinic crystal structure remains stable up to decomposition (Figure 4a). This is also counterparted by the essentially flat TG and DSC curves presented in the Supporting Information (Figure S2). For the α-$(PRSH)_3Bi_2X_9$ phases, a progressive change associated with thermal expansion is visible in Figure 4b,c, followed by the merging of several couples of peaks, in line with a second-order phase transition (where a new state of increased symmetry develops continuously from the low temperature phase), leading to

monoclinic polymorphs of *C2/m* symmetry. Their complete and complementary TG/DSC analysis is presented and discussed in detail in the Supporting Information (Figure S3). In the β-polymorphs, *all* three PRSH cations (which, in the triclinic α-phases, are in general positions) end up in special positions: one lying flat on a mirror plane, the other two normal to it. Simultaneously, also the $[Bi_2X_9]^{3-}$ anions slightly reorient, and become bisected by a crystallographic mirror plane *not* relating the two Bi^{3+} ions. Note that symmetrization of the different moieties in the *C2/m* space group does not require such a synchronized positioning *on mirror planes*, as twofold axes, for both anions (of idealized D_{3h} symmetry) and cations (of idealized C_{2v} symmetry), may equally hold. Indeed, up to 20 distinct combinations of different Wyckoff positions (of *2* or *m* symmetry for $[Bi_2X_9]^{3-}$, and *1*, *2* or *m* symmetry for PRSH, including also the presence of one fully independent cation jointly to one on a special position), are possible. If they were labeled by the (x,y,z,t) (where x,y,z,t = *1*, *2* or *m*) or (x,*1*,z) (where x,z = *1, 2* or *m*) genes, then the α- to β-phase transformation would be best described by a remarkable (*1,1,1,1*) to (*m,m,m,m*) symmetry change.

For all three species under study, refinement of cell parameters at different temperatures allowed the anisotropic thermal expansion coefficients κ_p to be derived (Table 2), using their relative variations, $\Delta p/p_0$, with p = lattice parameters and cell volume, p_0 being the reference value at room temperature. The $\Delta p/p_0 = \kappa_p \Delta T$ values are plotted in Figure 5 as a function of the temperature, jointly with the visualization of the thermal strain tensors derived therefrom (using Ohashi's approach[39] and the Wintensor program[40]). Figure S4 shows the thermal strain tensors for the high-temperature β-phases.

A quick glance on the κ_p values included in Table 2 for the monoclinic (PRSH)$BiCl_4$ phase clearly suggests a than the maximum thermal strain occurs along the unique axis **b**, with more limited expansion in the **a** and **c** directions. However, due to a substantial flexibility of the β angle, there appears to be a stiff direction (roughly oriented along **a**+**c**) where thermal expansion is very low (see Figure 5b). The analysis of the intermolecular contacts, apparently, does not explain this fact, which,

therefore, we phenomenologically describe by the concurrence of both transversal (along **a**) and longitudinal (along **c**) expansion of the $[BiCl_4]_\infty$ polyanions with their lateral sliding (increasing the β angle).

The two isomorphous structures of α-$(PRSH)_3Bi_2X_9$ (X = Br, I) show also very similar trend in lattice parameter evolution. Apart from the phase transformation temperature (lower in the bromide than in the iodide species) and from their different reversibility aspects (which we attribute to kinetic effects once temperature is decreased from 110°, or 190°C, respectively), the thermal expansion coefficients and the thermal tensors are very similar (see Figure 5c-f). They clearly manifest nearly null thermal strain in the *ab* plane, counterparted by the maximum expansion (approximately) in the **b** direction. We attribute this experimental evidence by the tendency of two (out of three) PRSH cations to reorient themselves in a way that they progressively adopt a configuration normal to the crystallographic mirror plane (eventually ending in the monoclinic β-phase, where *b* is expanded by more than 3%). As a final comment, the volumetric thermal expansion coefficients, κ_V, of the three species, and of the β-phases as well (the slope of the blue-circles lines in Figure 5a,c,e) are practically identical, suggesting an overall similarity and relative stiffness of intermolecular contacts in the 1D polymeric and 0D materials.

Table 2. Linear thermal expansion coefficients, for cell axes, interaxial angles and cell volume.

Species	$(PRSH)BiCl_4$	α-$(PRSH)_3Bi_2Br_9$	α-$(PRSH)_3Bi_2I_9$
κ_a, MK^{-1}	25	16	22
κ_b, MK^{-1}	64	82	74
κ_c, MK^{-1}	24	24	15
κ_α, MK^{-1}		51	46
κ_β, MK^{-1}	43	-17	-11
κ_γ, MK^{-1}		-9	-14
κ_V, MK^{-1}	119	129	116

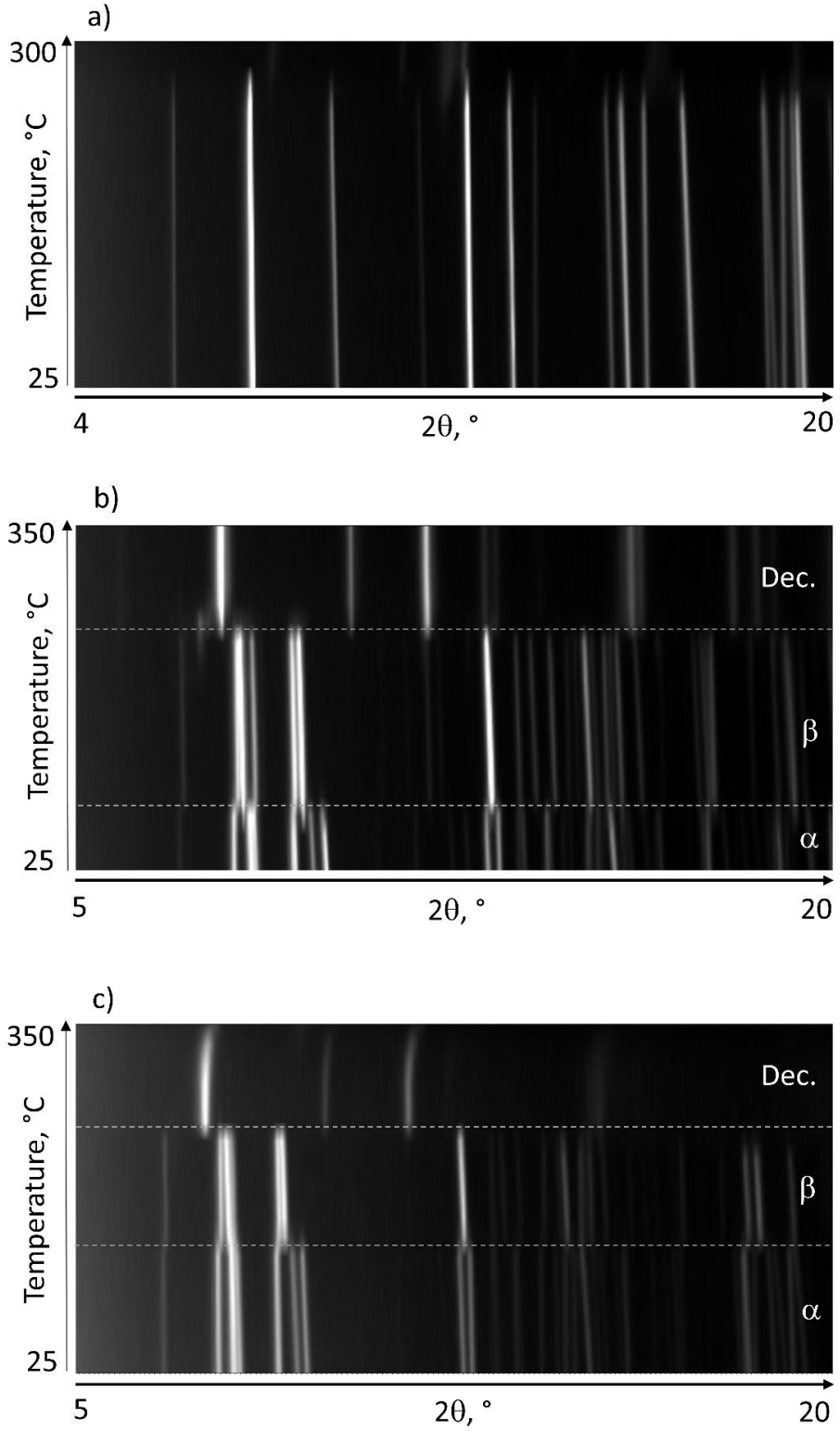

Figure 4. VT-XRD plots for a) (PRSH)$BiCl_4$, b) $(PRSH)_3Bi_2Br_9$ and c) $(PRSH)_3Bi_2I_9$.

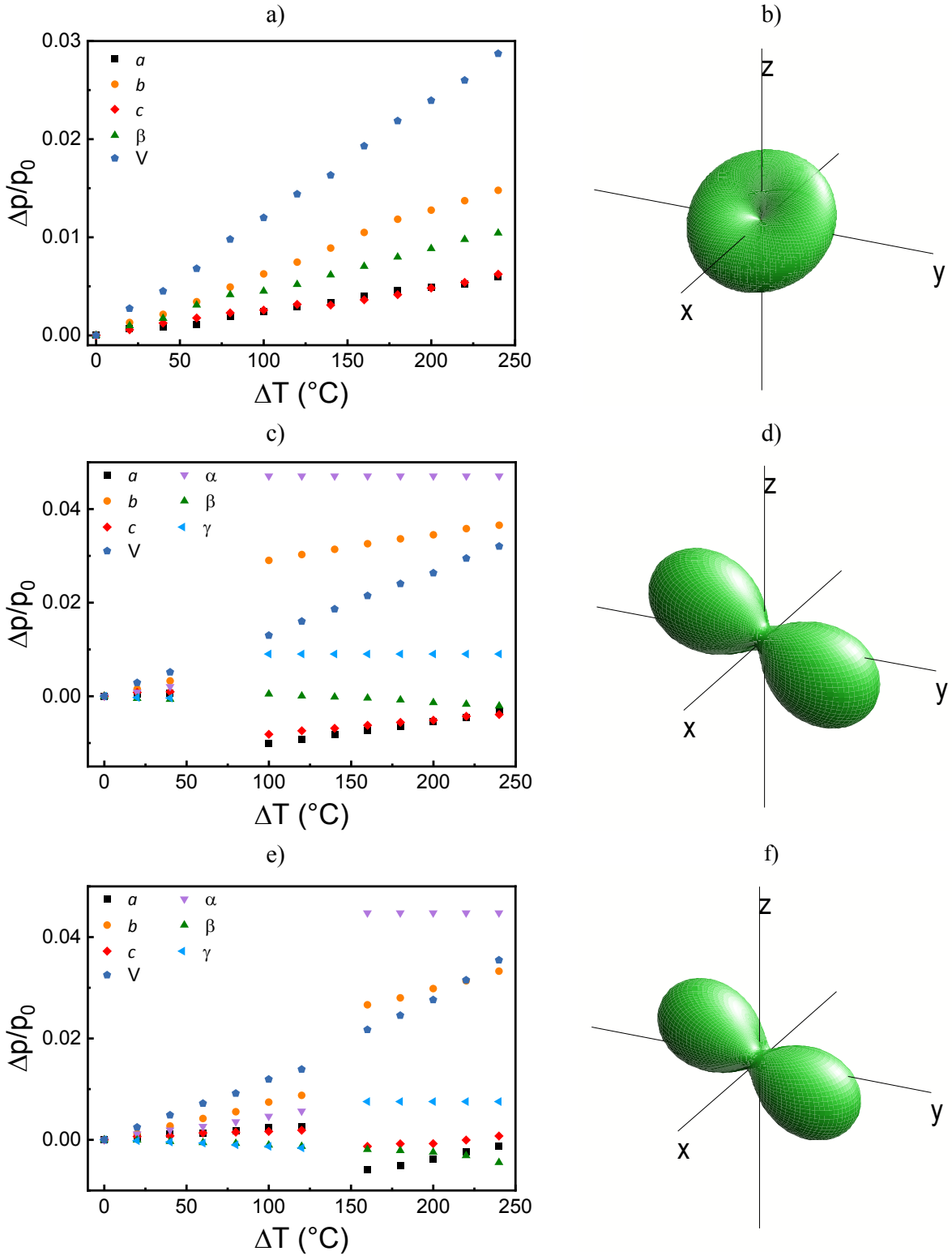

Figure 5. Left: the thermal evolution of the lattice parameters, expressed as $\Delta p/p_0$ (see text). Right; visualization of the strain tensors derived therefrom. a,b): (PRSH)$BiCl_4$. c,d) and e,f): α-$(PRSH)_3Bi_2X_9$ (X = Br, I, respectively). All tensors are drawn at the same scale. In c) and e), the constancy of the α and γ angles (blue and magenta triangles) reflect the *C2/m* monoclinic symmetry.

3.4 Electronic band structure

All band structures for the investigated compounds show direct band gaps at the Γ point, with values between 2 and 3 eV. As expected, the band gap follows the usual trend observed in lead halide perovskites: Cl > Br > I. The valence and conduction bands are flat, which is also expected in one- or zero-dimensional compounds with significant localization, since they arise from the overlap of Bi and halide orbitals. While the effective mass of electrons, that is proportional to the inverse of the band curvature, is therefore generally high, it also follows the trend Cl > Br > I, indicating in principle more favorable conditions for electron mobility in α-$(PRSH)_3Bi_2I_9$ than in the lighter halide phases.

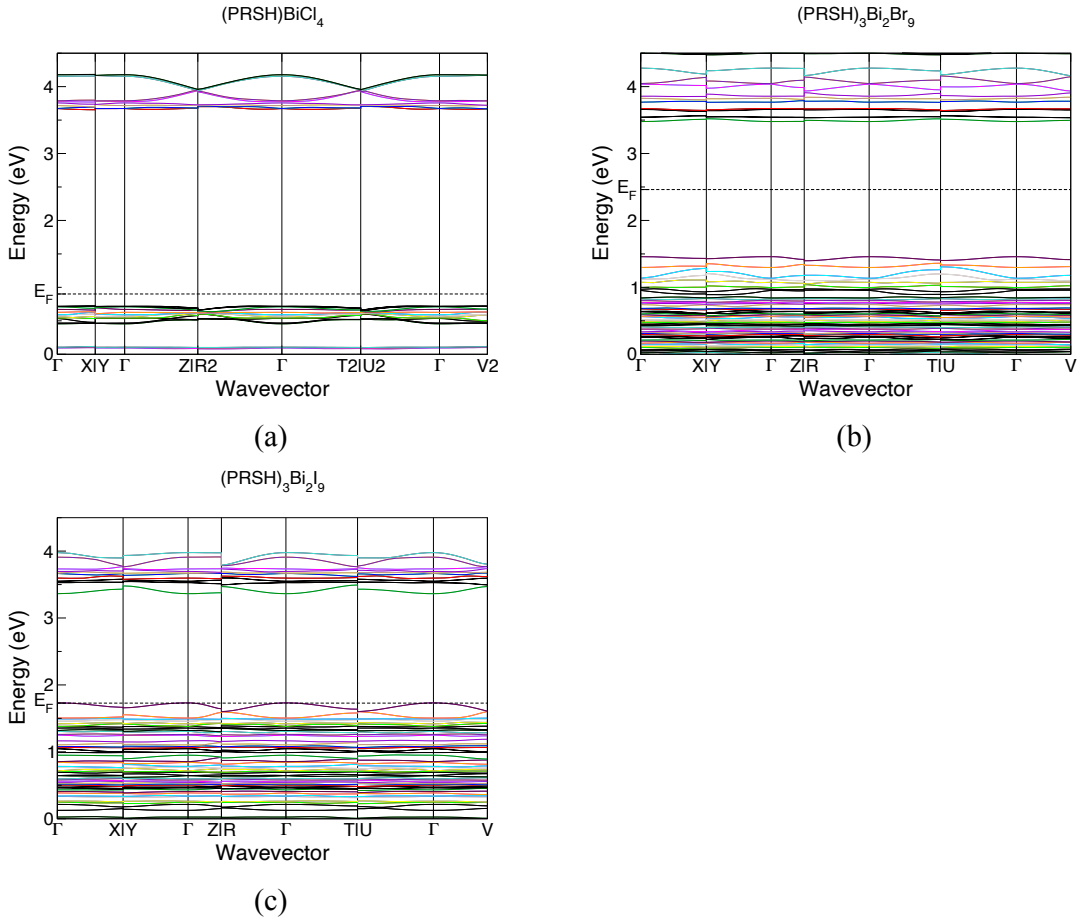

Figure 6 – Band structure of $(PRSH)BiCl_4$, α-$(PRSH)_3Bi_2Br_9$ and α-$(PRSH)_3Bi_2I_9$.

4. Conclusion

We have prepared three new halobismutate species with the rigid and chemically stable protonated proton-sponge cation, which showed a versatile crystal chemistry. In the absence of single

crystals of suitable size and quality, their complex crystal structures have been determined by synchrotron X-rays powder diffraction methods. The only polymeric species, the chloride derivative, shows a zigzagging sequence of edge-sharing $BiCl_6$ octahedra and is fully silent when heated up to decomposition. At variance, the isostructural bromide and iodide derivatives contain isolated $[Bi_2X_9]^{3-}$ anions and show phase transformations into the high-temperature β-polymorphs, paralleled by comparable thermal strain coefficient and tensors. These transformations are attributed to slight reorientation of the all PRSH and metal complex ions and result in four molecular entities *all* lying on a special symmetry position, of the *m* type. The electronic band structures were computed *ab-initio* including relativistic spin-orbit coupling, and confirmed the occurrence of a direct band gap that decreases with increasing halide mass, regardless of the molecular connectivity. Work can be anticipated in the direction of inserting isovalent doping cations or in preparing mixed-halide species, towards fine-tuning of the spectroscopic, thermal and structural properties.

Acknowledgements

The authors thank the Italian Ministry of Research for partial funding (Project PRIN 2017L8WW48, HY-TEC. Hybrid ThermoElectric Composites: Proof-of-concepts for low-T, *n*-type and flexible thermoelectrics) and the University of Insubria for a Junior Assignee Grant. We acknowledge the CINECA award under the ISCRA initiative for the availability of high-performance computing resources and support (Project IsC91_DoPe). We heartily thank Dr. A. Cervellino for assistance during synchrotron X-ray powder diffraction measurements and Dr. A. Guagliardi for fruitful discussions.

Appendix A. Supporting Information.

Supporting Information includes the CIF file for the three room-temperature structures, Rietveld refinement plots, TG and DSC plots, visualization of the thermal strain tensors and crystal data for the high-temperature β-$(PRSH)_3Bi_2X_9$ phases. Supplementary data associated with this article can be found in the online version at doi:***/***.

References

[1] M. Grätzel, The Rise of Highly Efficient and Stable Perovskite Solar Cells, Acc, Chem. Res. 50 (2017) 487–491. https://dx.doi.org/10.1021/acs.accounts.6b00492.

[2] J. Huang, Y. Yuan, Y. Shao, Y. Yan, Understanding the physical properties of hybrid perovskites for photovoltaic applications. Nat. Rev. Mater. 2, (2017) 17042. https://dx.doi.org/10.1038/natrevmats.2017.42.

[3] S. Das, S. Gholipour, M. Saliba, The Versatile Application Range of Perovskite Optoelectronics. Energy Environ. Mat. 2 (2019) 144–151. https://dx.doi.org/10.1002/eem2.12044.

[4] Y.-H. Kim, H. Cho, T.-W. Lee, Metal halide perovskite light emitters. Proc. Nat. Acad. Sci. (2016) 201607471. https://dx.doi.org/10.1073/pnas.1607471113.

[5] M. Shellaiah, K. W. Sun, Review on Sensing Applications of Perovskite Nanomaterials. Chemosensors, 8 (2020) 55. https://dx.doi.org/10.3390/chemosensors8030055.

[6] Y. Fu, H. Zhu, H., J. Chen, J., M. P. Hautzinger, X.-Y. Zhu, S. Jin, Metal halide perovskite nanostructures for optoelectronic applications and the study of physical properties. Nat. Rev. Mater. 4 (2019) 169–188. https://dx.doi.org/10.1038/s41578-019-0080-9.

[7] T. Oku, Crystal structures of perovskite halide compounds used for solar cells, Rev. Adv. Mater. Sci. 59 (2020) 264-305. https://dx.doi.org /10.1515/rams-2020-0015.

[8] J. Jiang, F. Liu, I. Tranca, Q. Shen, S.Tao, Atomistic and Electronic Origin of Phase Instability of Metal Halide Perovskites. ACS Appl. Energy Mater. 3 (2020) 11548–11558. https://dx.doi.org /10.1021/acsaem.0c00791.

[9] K. Hong, Q. V. Le, S. Y. Kim, H. W. Jang, Low-dimensional halide perovskites: review and issues. J. Mater. Chem. C, 6 (2018) 2189-2209. https://dx.doi.org/10.1039/c7tc05658c

[10] Y. Chen, Y. Sun, J. Peng, J. Tang, K. Zheng, Z. Liang, 2D Ruddlesden-Popper Perovskites for Optoelectronics. Adv. Mater. 30 (2018) 1703487. https://dx.doi.org/10.1002/adma.201703487.

[11] H. Fu, Dion–Jacobson halide perovskites for photovoltaic and photodetection applications. J. Mater. Chem. C, 9 (2021), 6378–6394. https://dx.doi.org/10.1039/d1tc01061a.

[12] S. F. Hoefler, G. Trimmel, T. Rath, Progress on lead-free metal halide perovskites for photovoltaic applications: a review. Monatsh. Chem. 148 (2017) 795–826. https://dx.doi.org/10.1007/s00706-017-1933-9.

[13] J. S. Adjogri, E. L. Meyer, A Review on Lead-Free Hybrid Halide Perovskites as Light Absorbers for Photovoltaic Applications Based on Their Structural, Optical, and Morphological Properties. Molecules, 25 (2020), 5039. https://dx.doi.org/10.3390/molecules25215039.

[14] N. Zubkova, I, Pekov, D. Pushcharovsky, A review of crystal chemistry of natural silicates of alkaline elements in the light of new structural data. Miner. Magaz. 78 (2014) 253-265. https://dx.doi.org/10.1180/minmag.2014.078.2.03.

[15] L. Xu, Leimeng; S. Yuan, H. Zeng, J. Song. A comprehensive review of doping in perovskite nanocrystals/quantum dots: evolution of structure, electronics, optics and light-emitting diodes. Materials Today Nano 6 (2019), 100036. https://dx.doi.org/10.1016/j.mtnano.2019.100036

[16] L. Protesescu, S. Yakunin, S. Kumar, J. Bär, F. Bertolotti, N. Masciocchi, A. Guagliardi, M. Grotevent, I. Shorubalko, M.I. Bodnarchuk, C.J. Shih, M.V. Kovalenko, Dismantling the "Red Wall" of Colloidal Perovskites: Highly Luminescent Formamidinium and Formamidinium-Cesium Lead Iodide Nanocrystals. ACS Nano. 11 (2017) 3119-3134. https://dx.doi.org/10.1021/acsnano.7b00116.

[17] C. Pipitone, F. Giannici, A. Martorana, F. Bertolotti, G. Calabrese, S. Milita, A. Guagliardi, N. Masciocchi, Proton sponge lead halides containing 1D polyoctahedral chains. CrystEngComm, 23 (2021) 1126–1139. https://dx.doi.org/10.1039/d0ce01695k.

[18] C. Pipitone, F. Giannici**,** A. Martorana, G. García-Espejo, S. Carlotto, M. Casarin, A. Guagliardi, N. Masciocchi, Heterovalent Bi^{III}/Pb^{II} Ionic Substitution in One-Dimensional Trimethylsulfoxonium Halide Pseudo-Perovskites (X = I, Br), J. Phys. Chem. C 125 (2021) 11728–11742, https://dx.doi.org/10.1021/acs.jpcc.1c02571.

[19] S. Attique, N. Ali, S. Ali, R. Khatoon, N. Li, A. Khesro, S. Rauf, S. Yang, H. Wu, A Potential Checkmate to Lead: Bismuth in Organometal Halide Perovskites, Structure, Properties, and Applications. Adv. Sci., 7 (2020) 1903143. https://dx.doi.org/10.1002/advs.201903143.

[20] S. Wu, R. Chen, S. Zhang, B. H. Babu, Y. Yue, H. Zhu, Z. Yang, C. Chen, W. Chen, Y. Huang, S. Fang, T. Liu, L. Han, W. Chen, A chemically inert bismuth interlayer enhances long-term stability of inverted perovskite solar cells. Nat. Commun. 10 (2019) 1161. https://dx.doi.org/10.1038/s41467-019-09167-0.

[21] H.Y. Chen, L. Wu, C. Ren, Q.Z. Luo, Z.H. Xie, X. Jiang, S.P. Zhu, Y.K .Xia, Y.R. Luo, The effect and mechanism of bismuth doped lead oxide on the performance of lead-acid batteries. 95 (2001) 108–118. https://dx.doi.org/10.1016/S0378-7753(00)00640-6.

[22] S. Rieger, B. J. Bohn, M. Döblinger, A. F. Richter, Y. Tong, K. Wang, P. Müller-Buschbaum, L. Polavarapu, L. Leppert, J. K. Stolarczyk, J. Feldmann, Excitons and narrow bands determine the optical properties of cesium bismuth halides, Phys. Rev. B 100 (2019) 201404. https://dx.doi.org/10.1103/PhysRevB.100.201404.

[23] J. K. Pious, M. G. Basavarajappa, C. Muthu, R. Nishikubo, A. Saeki, S. Chakraborty, A. Takai, M. Takeuchi, C. Vijayakumar, Self-Assembled Organic Cations-Assisted Band-Edge Tailoring in Bismuth-Based Perovskites for Enhanced Visible Light Absorption and Photoconductivity, J. Phys. Chem. Lett. 12 (2021) 5758–5764. https://doi.org/10.1021/acs.jpclett.1c01321.

[24] J. Tauc, Optical properties and electronic structure of amorphous Ge and Si. Mater. Res. Bull. 3 (1968) 37–46. https://dx.doi.org/10.1016/0025-5408(68)90023-8.

[25] Willmott, P. R.; Meister, D.; Leake, S. J.; Lange, M.; Bergamaschi, A.; Böge, M.; Calvi, M.; Cancellieri, C.; Casati, N.; Cervellino, A.; Chen, Q.; David, C.; Flechsig, U.; Gozzo, F.; Henrich, B.; Jäggi-Spielmann, S.; Jakob, B.; Kalichava, I.; Karvinen, P.; Krempasky, J.; Lüdeke, A.; Lüscher, R.; Maag, S.; Quitmann, C.; Reinle-Schmitt, M. L.; Schmidt, T.; Schmitt, B.; Streun, A.; Vartiainen, I.; Vitins, M.; Wang, X.; Wullschleger, R. The Materials Science beamline upgrade at the Swiss Light Source. Journal of Synchrotron Radiation, 20 (2013) 667–682. https://dx.doi.org 10.1107/s0909049513018475.

[26] A. Bergamaschi, A. Cervellino, R. Dinapoli, F. Gozzo, B. Henrich, I. Johnson, P. Kraft, A. Mozzanica, B. Schmitt, X. Shi, The MYTHEN detector for X-ray powder diffraction experiments at the Swiss Light Source, J. Synchr. Rad. 17 (2010) 653-668. https://dx.doi.org/ 10.1107/S0909049510026051

[27] A.A. Coelho, Indexing of powder diffraction patterns by iterative use of singular value decomposition, J. Appl. Cryst. 36 (2003) 86-95. https://dx.doi.org/10.1107/S0021889802019878.

[28] TOPAS-R, V.3 (2005), Bruker AXS, Karlsruhe, Germany.

[29] P. Giannozzi, S. Baroni, N. Bonini, M. Calandra, R. Car, C. Cavazzoni, D. Ceresoli, G. L. Chiarotti, M. Cococcioni, I. Dabo, A. Dal Corso, S. de Gironcoli, S. Fabris, G. Fratesi, R. Gebauer, U. Gerstmann, C. Gougoussis, A. Kokalj, M. Lazzeri, L. Martin-Samos, N. Marzari, F. Mauri, R. Mazzarello, S. Paolini, A. Pasquarello, L. Paulatto, C. Sbraccia, S. Scandolo, G. Sclauzero, A. P. Seitsonen, A. Smogunov, P. Umari, R. M. Wentzcovitch, QUANTUM ESPRESSO: A Modular and Open-Source Software Project for Quantum Simulations of Materials, J. Phys.: Condens. Matter 21 (2009) 395502. https://dx.doi.org/10.1088/0953-8984/21/39/395502.

[30] P. Giannozzi, O. Baseggio, P. Bonfà, D. Brunato, R. Car, I. Carnimeo, C. Cavazzoni, S. de Gironcoli, P. Delugas, F. Ferrari Ruffino, A. Ferretti, N. Marzari, I. Timrov, A. Urru, S. Baroni, Quantum ESPRESSO toward the Exascale, J. Chem. Phys. 152 (2020) 154105. https://dx.doi.org/10.1063/5.0005082.

[31] P. Giannozzi, O. Andreussi, T. Brumme, O. Bunau, M. Buongiorno Nardelli, M. Calandra, R. Car, C. Cavazzoni, D. Ceresoli, M. Cococcioni, N. Colonna, I. Carnimeo, A. Dal Corso, S. de Gironcoli, P. Delugas, R. A. DiStasio, A. Ferretti, A. Floris, G. Fratesi, G. Fugallo, R. Gebauer, U. Gerstmann, F. Giustino, T. Gorni, J. Jia, M. Kawamura, H.-Y. Ko, A. Kokalj, E. Ku¨çu¨kbenli, M. Lazzeri, M. Marsili, N. Marzari, F. Mauri, N. L. Nguyen, H.-V. Nguyen, A. Otero-de-la-Roza, L. Paulatto, S. Ponc´e, D. Rocca, R. Sabatini, B. Santra, M. Schlipf, A. P. Seitsonen, A. Smogunov, I. Timrov, T. Thonhauser, P. Umari, N. Vast, X. Wu and S. Baroni, Advanced Capabilities for Materials Modelling with Quantum ESPRESSO, J. Phys.: Condens. Matter 29 (2017) 465901. https://dx.doi.org/10.1088/1361-648X/aa8f79.

[32] J. P. Perdew, K. Burke, M. Ernzerhof, Generalized Gradient Approximation Made Simple, Phys. Rev. Lett., 77 (1996) 77, 3865–3868. https://dx.doi.org/10.1103/PhysRevLett.77.3865.

[33] Y. Hinuma, G. Pizzi, Y. Kumagai, F. Oba, I. Tanaka, Band structure diagram paths based on crystallography, Comp. Mater. Sci. 128 (2017) 140-184. https://dx.doi.org/ 10.1016/j.commatsci.2016.10.015.

[34] G. Xu, Y. Li, W.-W. Zhou, G.-J. Wang, X.-F. Long, L.-Z. Cai, M.-S. Wang, G.-C. Guo, J.-S. Huang, G. Bator, R. Jakubas, A ferroelectric inorganic–organic hybrid based on NLO-phore stilbazolium. J. Mater. Chem., 19 (2009) 2179-2183. https://dx.doi.org10.1039/b819473d.

[35] B.Blazic, F.Lazarini, Structure of diethylammonium tetrachlorobismuthate(III), Acta Cryst. C, 41 (1985) 519-521. https://dx.doi.org/10.1107/S0108270185008782.

[36] N. D. Kushch, A. A. Dyachenko, V. V. Gritsenko, P. Cassoux, C. Faulmann, A. Kobayashi, H. Kobayashi, Two new cation radical bis(ethylenedithio)tetraselenafulvalene (BETS) salts, α-$(BETS)_6Bi_3Cl_{12}\cdot PhCl$ and $(BETS)_2Bi_2Cl_8$: synthesis, structure and conducting properties. First characterisation of the new trinuclear anion $[Bi_3Cl_{12}]^{3-}$, J. Chem. Soc., Dalton Trans., (1998) 683-688. https://dx.doi.org/10.1039/A705223E.

[37] M. Bujak, Understanding distortions of inorganic substructures in chloridobismuthates(III), Acta Cryst. B 77 (2021) 763-771. https://doi.org/10.1107/S2052520621004753.

[38] D. H. Fabini, R. Seshadri, M. G. Kanatzidis, (2021). The underappreciated lone pair in halide perovskites underpins their unusual properties, MRS Bulletin, 45 (2021) 467–477. https://dx.doi.org/10.1557/mrs.2020.142.

[39] Y. Ohashi, STRAIN: A Program to Calculate the Strain Tensor from Two Sets of Unit-Cell Parameters, in Comparative Crystal Chemistry, R. M. Hazen, L. W. Finger Eds., Wiley, 1982, pp. 92–102.

[40] WinTensor, Tensor-Drawing and Calculation Tool for Windows 9598NT2000XP, University of Washington, Seattle, USA.